SANDIA REPORT

SAND2013-5484
Unlimited Release
Printed July 2013

Reducing Uncertainty in High-Resolution Sea Ice Models

Kara Peterson, Pavel Bochev

Prepared by
Sandia National Laboratories
Albuquerque, New Mexico 87185 and Livermore, California 94550

Sandia National Laboratories is a multi-program laboratory managed and operated by Sandia Corporation, a wholly owned subsidiary of Lockheed Martin Corporation, for the U.S. Department of Energy's National Nuclear Security Administration under contract DE-AC04-94AL85000.

Sandia National Laboratories

Issued by Sandia National Laboratories, operated for the United States Department of Energy by Sandia Corporation.

Available to DOE and DOE contractors from
U.S. Department of Energy
Office of Scientific and Technical Information
P.O. Box 62
Oak Ridge, TN 37831

Telephone: (865) 576-8401
Facsimile: (865) 576-5728
E-Mail: reports@adonis.osti.gov
Online ordering: http://www.osti.gov/bridge

Available to the public from
U.S. Department of Commerce
National Technical Information Service
5285 Port Royal Rd
Springfield, VA 22161

Telephone: (800) 553-6847
Facsimile: (703) 605-6900
E-Mail: orders@ntis.fedworld.gov
Online ordering: http://www.ntis.gov/help/ordermethods.asp?loc=7-4-0#online

SAND2013-5484
Unlimited Release
Printed July 2013

Reducing Uncertainty in High-Resolution Sea Ice Models

Kara Peterson
Numerical Analysis and Applications
Sandia National Laboratories
P.O. Box 5800
Albuquerque, NM 87185-1318
kjpeter@sandia.gov

Pavel Bochev
Numerical Analysis and Applications
Sandia National Laboratories
P.O. Box 5800
Albuquerque, NM 87185-1320
pbboche@sandia.gov

Abstract

Arctic sea ice is an important component of the global climate system, reflecting a significant amount of solar radiation, insulating the ocean from the atmosphere and influencing ocean circulation by modifying the salinity of the upper ocean. The thickness and extent of Arctic sea ice have shown a significant decline in recent decades with implications for global climate as well as regional geopolitics. Increasing interest in exploration as well as climate feedback effects make predictive mathematical modeling of sea ice a task of tremendous practical import.

Satellite data obtained over the last few decades have provided a wealth of information on sea ice motion and deformation. The data clearly show that ice deformation is focused along narrow linear features and this type of deformation is not well-represented in existing models. To improve sea ice dynamics we have incorporated an anisotropic rheology into the Los Alamos National Laboratory global sea ice model, CICE. Sensitivity analyses were performed using the Design Analysis Kit for Optimization and Terascale Applications (DAKOTA) to determine the impact of material parameters on sea ice response functions. Two material strength parameters that exhibited the most significant impact on responses were further analyzed to evaluate their influence on quantitative comparisons between model output and data. The sensitivity analysis along with ten year model runs indicate that while the anisotropic rheology provides some benefit in velocity predictions, additional improvements are required to make this material model a viable alternative for global sea ice simulations.

Acknowledgment

Funding from Laboratory Directed Research and Development program is gratefully acknowledged. The authors would like to thank Elizabeth Hunke for valuable assistance with the CICE code and for providing external forcing files and Deborah Sulsky and Howard Schreyer for helpful discussions on the EDC rheology and its implementation in CICE.

Contents

Figures

Tables

Nomenclature

m - ice mass per unit area

$\mathbf{v}$ - ice velocity

$\boldsymbol{\tau}_a$ - atmospheric drag

$\boldsymbol{\tau}_w$ - ocean drag

ω - Earth's rotation

ϕ - latitude

$\boldsymbol{\sigma}$ - Cauchy stress tensor

$\mathbf{N}$ - depth integrated stress tensor

$\boldsymbol{\varepsilon}$ - strain tensor

E Young's modulus

μ bulk modulus

ν Poisson ratio

τ_t tangential traction

τ_{nf} tensile strength

τ_{tf} shear strength

s_m shear multiplication factor

f_c' compressive strength

$\mathbf{u}$ - ice displacement

$[\![\mathbf{u}]\!]$ displacement jump

η shear viscosity

ζ bulk viscosity

D_d divergence

D_v vorticity

D_s shear

1 Introduction

Arctic sea ice is an important component of the global climate system, reflecting a significant amount of solar radiation, insulating the ocean from the atmosphere and influencing ocean circulation by modifying the salinity of the upper ocean. The thickness and extent of Arctic sea ice have shown a significant decline in recent decades [3, 23]. This decline has implications for global climate, where new evidence suggests that reduction in Arctic sea ice can influence atmospheric circulation over the mid-latitudes [7], and for regional geopolitics, where disappearing sea ice has renewed interest in exploration and mineral extraction in the Arctic. For these reasons predictive sea ice modeling is a high priority.

Numerical modeling of sea ice is a complex multi-physics problem. Sea ice is mechanically driven by surface winds and ocean currents, which can open cracks or form pressure ridges under convergence. Additionally, sea ice grows and melts seasonally in response to incoming solar radiation, thermal radiation from the atmosphere, and heat flux from the ocean. A complete sea ice model must incorporate variations in ice thickness including ridges and cracks, the annual cycle of growth and melt due to radiative forcing, and mechanical deformation due to surface winds, ocean currents, and Coriolis forces.

Existing sea ice components of global climate models vary in their predictions for Arctic sea ice evolution, but most have significantly underestimated the rate of decline in minimum sea ice extent over the last thirty years [34]. Additionally, comparisons with satellite data show that models do not accurately represent sea ice drift or deformation [28]. There are multiple contributing factors for these discrepancies, which can include errors in atmospheric and ocean forcing [17], however, it has become clear that one limitation of existing sea ice models is in the rheology that describes the internal forcing component of the equations of motion.

The standard isotropic rheology used in sea ice simulations is the viscous-plastic model developed by Hibler [12]. At the time the rheology was developed, resolutions in sea ice calculations were limited to scales of O(100 km). At these scales it is reasonable to assume that cracks in the ice, known as leads, are distributed randomly over a region so that their effect can be approximated by an isotropic weakening. However, at current high-resolutions of O(10 km), a single lead can dominate a region producing deformation that is highly anisotropic [4]. Satellite data clearly show that deformation in the ice is focused along narrow linear features that are likely associated with leads or systems of leads. Comparisons between model predictions of deformation and satellite data show significant discrepancies [22]. Additionally, analysis of the spatial scaling of the deformation supports the view that isotropic rheologies are not accurately capturing the deformation [33, 10].

To improve the representation of sea ice dynamics a number of anisotropic constitutive models have been developed for sea ice [5, 38, 9]. Our work will utilize the elastic-decohesive rheology developed by Schreyer [31]. This rheology explicitly models the formation and evolution of cracks in the ice and is inherently anisotropic. This constitutive model was previously incorporated into a material-point method sea ice model where promising results were seen for regional simulations [36, 35]. This rheology has now been added to CICE, the Los Alamos sea ice model [16], which is a global sea ice model that is a component of the Community Earth System Model (CESM). Section 2 describes the governing equations for sea ice dynamics and compares the elastic-decohesive rheology (EDC) to the default elastic-viscous-plastic (EVP) rheology used in CICE. Section 3 details the implementation of EDC in CICE.

The elastic-decohesive rheology contains a number material parameters that are constrained by data, but have exact values that are uncertain. After implementation of the model in CICE, a sensitivity analysis has been performed to determine the most important rheology parameters for a set of response functions that included global ice quantities like total Arctic ice volume as well as parameters that assess the performance of the model in comparison with satellite deformation data. Details of this analysis are provided in Section 4. The two most important rheologic parameters were then used in an additional study to improve the match of model output to ice motion and deformation measures described in Section 5. Finally, results of ten year CICE simulations with the EDC rheology and the EVP rheology, which were done to assess model performance for longer time frames, are given in Section 6.

2 Sea Ice Dynamics

Sea ice dynamics are governed by a linear momentum equation for the two-dimensional spatially and temporally varying ice velocity $\mathbf{v}$. Due to the large extent to thickness ratio of sea ice a shallow ice formulation is used, which can be obtained by integrating the full three-dimensional sea ice momentum equation over thickness [11]. The resulting equation, which balances sea ice forces per unit area, is of the form

$$m\frac{\partial \mathbf{v}}{\partial t} = \nabla \cdot \mathbf{N} + \mathbf{t}_a + \mathbf{t}_w - \mathbf{f}_c - m\mathbf{g}\nabla H \tag{1}$$

where m is the mass per unit area of ice and snow. External forces acting on the ice include the atmospheric drag ($\mathbf{t}_a$), the ocean drag ($\mathbf{t}_w$), the Coriolis force ($\mathbf{f}_c$), and the sea surface tilt force ($m\mathbf{g}\nabla H$), which depends on the gradient of the sea surface height (H) and the acceleration due to gravity ($\mathbf{g}$). The Coriolis force

$$\mathbf{f}_c = 2\rho\bar{h}\omega \sin\phi(\hat{\mathbf{k}} \times \mathbf{v}) \tag{2}$$

is a function the Earth's rotation (ω) and the latitude (ϕ) where $\hat{\mathbf{k}}$ is the unit vector in the vertical direction. The ocean drag is typically given by a quadratic law

$$\boldsymbol{\tau_w} = c_w\rho_w\|\mathbf{v} - \mathbf{v}_w\|(\mathbf{v} - \mathbf{v}_w) \tag{3}$$

where ρ_w is the ocean density, $\mathbf{v}_w$ is the two-dimensional ocean velocity, and c_w is the ocean drag coefficient. In many sea ice models a quadratic drag law is also used for the atmospheric drag term, however, the LANL CICE code contains an atmospheric boundary layer routine where the atmospheric drag is calculated based on turbulent scales for the velocity [16]. The drag force due to atmospheric winds is the dominant external forcing on the ice.

The internal force ($\nabla \cdot \mathbf{N}$) depends on the depth-integrated stress tensor $\mathbf{N}$, which is obtained from the rheology that relates stress to strain or strain rate. Most sea ice models use variations on the viscous-plastic rheology developed by Hibler [12]. For this analysis we are using an elastic-decohesive rheology developed by Schreyer and others [31] and an elastic-viscous-plastic rheology, which is a modification of the viscous-plastic rheology and is the default rheology in CICE [13]. Details of both rheologies are provided in Subsections 2.1 and 2.2.

Sea ice dynamics are coupled to the thermodynamics through an ice thickness distribution, which accounts for the sub-grid scale variations in thickness in the model [37]. Changes in ice thickness due to thermodynamic growth or melt are obtained from an energy-conserving thermodynamic model that involves the solution of a one-dimensional temperature equation for the ice [2]. These thickness changes affect the dynamics through the mass per unit area (m) in the momentum equation, which is computed from the ice thickness distribution, and through a dependence of the rheology on ice thickness. Changes to thickness due to mechanical ridging are determined from a ridging equation that depends on ice divergence and shear derived from the ice motion [30]. For more details on the full set of sea ice governing equations see [27, 16].

2.1 Elastic-Viscous-Plastic Rheology

The elastic-viscous plastic (EVP) rheology is a modification to the viscous-plastic rheology, where ice behavior is based on a rigid plastic model [12, 13]. The plastic behavior is defined by a yield curve in depth integrated stress space and associated flow rules for the strain rate. The

original viscous-plastic model uses an elliptical yield curve in principal depth integrated stress space of the form

$$F(N_1, N_2) = \left(\frac{N_1 + N_2 + P}{P}\right)^2 + \left(\frac{N_2 - N_1}{P} e\right)^2 - 1 \tag{4}$$

where N_1 and N_2 are the principal components of the depth integrated stress, e is the eccentricity of the elliptical yield curve and P is a measure of ice strength. A plot of the viscous-plastic yield curve is shown in Figure 1. The ice is constrained in stress space to lie on the curve where $F = 0$, which defines the plastic regime. In Hibler's original formulation, the ice strength P is taken to be

$$P = P^* h e^{-C(1-A)} \tag{5}$$

where h is the thickness, A is the compactness or fractional area covered by ice, and C and P^* are constants. The CICE code uses a more complex form of the strength that depends on the ridging algorithm and is documented in [26]. The two-dimensional strain rate tensor, $\dot{\boldsymbol{\varepsilon}}$ is defined as the symmetric part of the velocity gradient, which is equal to $1/2(\nabla \mathbf{v} + \nabla \mathbf{v}^T)$. The viscous-plastic constitutive law can be derived from the yield curve assuming the following normal flow rule for strain rate in principal coordinates

$$\dot{\varepsilon_1} = \omega \frac{\partial F}{\partial N_1} \quad \dot{\varepsilon_2} = \omega \frac{\partial F}{\partial N_2} \tag{6}$$

where ω is the plastic evolution parameter. For this rheology ω may be solved for directly and a closed form expression for the rheology is obtained as

$$\mathbf{N} = 2\eta \dot{\boldsymbol{\varepsilon}} + (\zeta - \eta)\mathrm{tr}(\dot{\boldsymbol{\varepsilon}})\mathbf{I} + \frac{P\mathbf{I}}{2} \tag{7}$$

where ζ is the bulk viscosity, η is the shear viscosity, and $\mathbf{I}$ is the two-dimensional identity tensor. Both ζ and η are functions of the strain rate, $\dot{\boldsymbol{\varepsilon}}$, and can be written as

$$\zeta = \frac{P}{2\Delta}, \qquad \eta = \frac{P}{2\Delta e^2} \tag{8}$$

for

$$\Delta = \left((\dot{\varepsilon}_{11}^2 + \dot{\varepsilon}_{22}^2)(1 + e^{-2}) + 4\dot{\varepsilon}_{12}^2 e^{-2} + 2\dot{\varepsilon}_{11}\dot{\varepsilon}_{22}(1 + e^{-2})\right)^{1/2}. \tag{9}$$

In this formulation the viscosity coefficients, ζ and η, can become arbitrarily large as the strain rate goes to zero. To remove this possibility, limiting values are set for the strain rates. When the limiting values are approached the ice behaves as a linearly viscous fluid undergoing slow creep. In the original formulation at small strain rates when the ice is approximately rigid, the stress lies on an elliptical surface concentric with the original yield surface in principal stress space, producing a nonzero stress state for a zero strain rate. A pressure replacement modification was introduced later to restrict the stress to zero for a zero strain rate [8].

An alternative method of regularizing the constitutive equation is due to Hunke and Dukowicz [13], who included an elastic component to control the behavior in the limit of infinite viscosity. The viscous plastic rheology can alternatively be written for strain rate as a function of depth integrated stress as

$$\dot{\boldsymbol{\varepsilon}} = \frac{1}{2\eta}\mathbf{N} + \frac{\eta - \zeta}{4\eta\zeta}\left(\mathrm{tr}\mathbf{N} + \frac{P}{4\zeta}\right)\mathbf{I}. \tag{10}$$

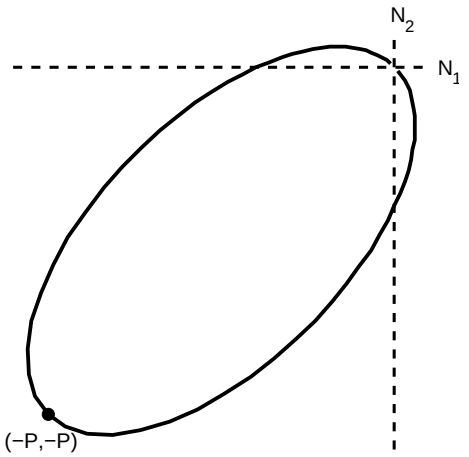

Figure 1: Elliptic yield curve used in the elastic-viscous plastic rheology. The ice strength P determines the size of the yield curve and depends on ice concentration and thickness.

The elastic-viscous-plastic rheology can be obtained by including a simple linear elastic relationship $\dot{\mathbf{N}} = E\dot{\boldsymbol{\varepsilon}}$ where E is a scalar elastic parameter. Combining this with the viscous-plastic constitutive model results in

$$\dot{\boldsymbol{\varepsilon}} = \frac{1}{2\eta}\mathbf{N} + \frac{\eta - \zeta}{4\eta\zeta}\left(\mathrm{tr}\mathbf{N} + \frac{P}{4\zeta}\right)\mathbf{I} + \frac{1}{E}\dot{\mathbf{N}}. \tag{11}$$

In the limit as $\eta, \zeta \to \infty$ the simple elastic equation is recovered and in the steady state limit the viscous-plastic relationship is recovered [13].

The EVP rheology is numerically efficient as it permits explicit solution of the dynamics. It is isotropic because the ice strength depends on ice concentration and thickness, but does not have a directional component. Leads in the ice can be inferred from areas of low ice concentration or small thickness, but are not explicitly modeled.

2.2 Elastic-Decohesive Rheology

In contrast to EVP the elastic-decohesive (EDC) rheology explicitly accounts for cracks or leads in the ice by modeling them as displacement discontinuities, while intact ice is assumed to behave elastically [31]. Assume we have a discontinuity on a surface Γ with a well-defined normal, $\mathbf{n}$. We regard the surface Γ as the level set of a C^1 function g, *i.e.* $\Gamma = \{\mathbf{x} : g(\mathbf{x}) = 0\}$. Define $\Omega_- = \{\mathbf{x} : g(\mathbf{x}) < 0\}$ and $\Omega_+ = \{\mathbf{x} : g(\mathbf{x}) > 0\}$. The domain is then decomposed into $\Omega = \Omega_- \cup \Gamma \cup \Omega_+$. Once a discontinuity forms the total displacement field $\mathbf{u}(\mathbf{x}, t)$ can be separated into a continuous component $\bar{\mathbf{u}}(\mathbf{x}, t)$ and a jump discontinuity $[\![\mathbf{u}]\!]$ in the form

$$\mathbf{u} = \overline{\mathbf{u}} + [\![\mathbf{u}]\!]H_\Gamma, \qquad H_\Gamma = \begin{cases} 0, & \text{if } \mathbf{x} \in \Omega_- \\ 1 & \text{if } \mathbf{x} \in \Omega_+ \cup \Gamma \end{cases}. \tag{12}$$

The jump in displacement has components $[\![\mathbf{u}]\!] = (u_n, u_t)$ in the local $\mathbf{n} - \mathbf{t}$ basis, where $\mathbf{t}$ is the tangent to the failure surface.

The EDC rheology is formulated using a failure surface in stress space, which bounds the elastic regime and defines the region where leads initiate. The failure surface F_n depends on components

of the Cauchy stress tensor $\boldsymbol{\sigma}$ along Γ. The traction on the failure surface has normal component $\tau_n = \mathbf{n} \cdot \boldsymbol{\sigma} \cdot \mathbf{n}$ and tangential component $\tau_t = \mathbf{t} \cdot \boldsymbol{\sigma} \cdot \mathbf{n}$. The remaining component of stress within the plane of the ice in this basis is the tangential stress, $\sigma_{tt} = \mathbf{t} \cdot \boldsymbol{\sigma} \cdot \mathbf{t}$. The EDC rheology combines brittle and shear failure with the transition zone between the two depending on the stress state of the material. The criterion for brittle failure is $B_n = 0$ where B_n is defined as

$$B_n = \frac{\tau_n}{\tau_{nf}} - f_n \left[1 - \frac{\langle -\sigma_{tt} \rangle^2}{f_c'^2} \right], \quad \text{where } \langle x \rangle \equiv \begin{cases} x & x \geq 0 \\ 0 & x < 0 \end{cases}. \tag{13}$$

For the case where $f_n = 1$ and $\sigma_{tt} \geq 0$, brittle failure occurs when the normal traction is equal to the tensile strength τ_{nf}. When σ_{tt} is compressive, brittle failure can occur for lower values of τ_n and the critical point depends on the material compressive strength f_c'. The brittle failure function is combined with a shear failure criterion in the full failure function

$$F_n(\boldsymbol{\sigma}) = \left(\frac{\tau_t}{s_m \tau_{tf}} \right)^2 + \mathrm{e}^{\kappa B_n} - 1. \tag{14}$$

The criterion for failure is then $F_n = 0$. If the normal component of traction has a large negative value ($\tau_n \to \infty$) and $\sigma_{tt} \geq 0$ implying that $B_n \to \infty$, then $F_n = 0$ when $\tau_t^2 = (s_m \tau_{tf})^2$. Therefore, $s_m \tau_{tf}$ is the failure stress in shear when the normal component of traction is large and compressive. In the case of pure shear failure where $\tau_n = 0$, $\sigma_{tt} = 0$, $f_n = 1$, and $B_n = -1$, we choose κ such that $\mathrm{e}^{-\kappa} = 1 - (\tau_{tf}^2/(s_m \tau_{tf})^2)$ so that pure shear failure occurs when $\tau_t = \tau_{tf}$.

The softening function f_n is equal to one when failure initiates and then reduces linearly as the crack opens and the normal displacement jump (u_n) increases with the form $f_n = \langle 1 - u_n/u_0 \rangle$. The crack is considered fully open when u_n equals the material parameter u_0 and the traction on the surface has reduced to zero. The crack orientation at initiation defined by the normal $\mathbf{n}$ is found by maximizing F_n over all possible crack orientations, which results in a failure function $F = max_n F_n$.

For this model a value of F less than zero indicates that the ice is in the elastic regime. Once failure occurs F is constrained to zero so that the stress state is maintained on the failure surface. A plot of $F = 0$ in principal stress space is shown in Figure 2. The arrows indicate the direction of failure with respect to principal stress. In the region where brittle stress dominates the normal to the failure surface is always in the direction of maximum principal stress. In the transition region and the shear region there are always two possible failure directions at angles $\pm\alpha$ with respect to the direction of maximum principal stress. The direction of rotation defined by the local vorticity determines which angle is chosen.

Once decohesion initiates the displacement discontinuity evolves according to a normal flow rule

$$[\![\dot{u}_n]\!] = \omega \frac{\partial F}{\partial \tau_n}, \quad [\![\dot{u}_s]\!] = \omega \frac{\partial F}{\partial \tau_t}. \tag{15}$$

In this case there is no closed form of the rheology so iterative methods are used to find the decohesive strain that satisfies $F(\boldsymbol{\sigma}) = 0$. In order to compute the stress we need the strain tensor defined as the symmetric part of the displacement gradient

$$\boldsymbol{\varepsilon} = \nabla^s \mathbf{u} = \bar{\boldsymbol{\varepsilon}} + ([\![\mathbf{u}]\!] \otimes \mathbf{n})^s \delta_\Gamma \tag{16}$$

where $\bar{\boldsymbol{\varepsilon}}$ is the regular or, in this case, the elastic portion of the strain, and δ_Γ is the delta function distribution on Γ. The superscript s denotes the symmetric part of the operator. The constitutive, stress-strain relation is then

$$\boldsymbol{\sigma} = \mathbb{E} : (\boldsymbol{\varepsilon} - ([\![\mathbf{u}]\!] \otimes \mathbf{n})^s \delta_\Gamma), \tag{17}$$

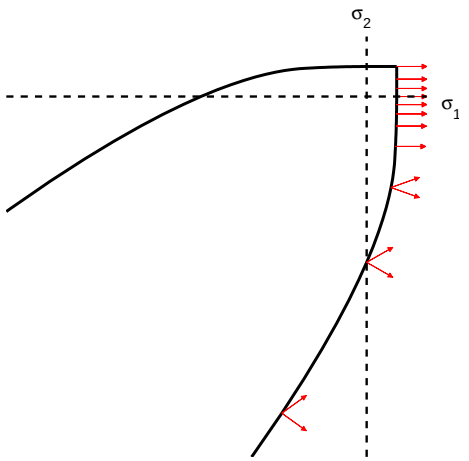

Figure 2: Failure curve in stress space used in the elastic-decohesive rheology. Arrows indicate the normal direction to the displacement discontinuity with respect to maximum principal stress.

where $\mathbb{E}$ is the standard fourth-order elasticity tensor. For isotropic elasticity, $\mathbb{E}$ can be represented by two independent material parameters, for example the shear modulus μ and the second Lame constant λ as

$$\mathbb{E}_{ijkl} = \lambda\delta_{ij}\delta_{kl} + 2\mu(\delta_{ik}\delta_{jl} + \delta_{il}\delta_{jk}) \tag{18}$$

where δ_{ij} is the Kronecker delta.

To integrate the EDC model stress back into the sea ice momentum equation, the Cauchy stress must be converted into a depth-integrated stress. To do this the depth-integrated stress is approximated as $\mathbf{N} = \int_0^{h_{max}} \boldsymbol{\sigma} dh \approx h\boldsymbol{\sigma}$.

3 Numerical Implementation in CICE

The incorporation of the EDC model into CICE was accomplished by substituting the discrete depth-integrated stress from ECD for the EVP discrete depth-integrated stress while maintaining existing methods for computing the discrete internal stress and momentum balance. Details of the numerical procedures used for the momentum balance solve in CICE can be found in [14]. The degrees-of-freedom in the CICE model are staggered so that velocities are located at cell corners and thermodynamic variables such as ice thickness distribution are located at cell centers [16]. Global ice simulations are typically performed on a displaced pole grid and therefore general curvilinear coordinates are used for the equations of motion.

In order to evalutate the EDC rheology we require values of the strain rate tensor defined as $\dot{\boldsymbol{\varepsilon}} = 1/2(\nabla\mathbf{v} + (\nabla\mathbf{v})^T)$. In two-dimensional general curvilinear coordinates the three distinct components of the strain rate tensor may be written as

$$\begin{aligned}
\dot{\varepsilon}_{11} &= \frac{1}{h_1}\frac{\partial u}{\partial \xi_1} + \frac{v}{h_1 h_2}\frac{\partial h_1}{\partial \xi_2} \\
\dot{\varepsilon}_{22} &= \frac{1}{h_2}\frac{\partial v}{\partial \xi_2} + \frac{u}{h_1 h_2}\frac{\partial h_2}{\partial \xi_1} \\
\dot{\varepsilon}_{12} = \dot{\varepsilon}_{21} &= \frac{1}{2}\left(\frac{h_1}{h_2}\frac{\partial}{\partial \xi_2}\left(\frac{u}{h_1}\right) + \frac{h_2}{h_1}\frac{\partial}{\partial \xi_2}\left(\frac{v}{h_2}\right)\right)
\end{aligned} \tag{19}$$

for nondimensional coordinates (ξ_1, ξ_2) and scale factors (h_1, h_2). In CICE the following bilinear form of the velocity $\mathbf{v} = (u, v)$ is assumed for each cell where superscripts ne, nw, se, sw denote cell corners [14]

$$\mathbf{v}(\xi_1, \xi_2) = \mathbf{v}^{ne}\xi_1\xi_2 + \mathbf{v}^{nw}(1-\xi_1)\xi_2 + \mathbf{v}^{sw}(1-\xi_1)(1-\xi_2) + \mathbf{v}^{se}\xi_1(1-\xi_2). \tag{20}$$

Using this bilinear form for the velocity, strain rates are evaluated at each of the four cell corners. Multiplying the strain rates by the time step (Δt) gives a value of strain increment for use in the EDC rheology. It is assumed in CICE that the scale factors (h_1, h_2) can be approximated as the mid cell lengths $(\bar{h}_1, \bar{h}_2)$. Additionally, the scale factor derivatives $(\partial h_1/\partial \xi_2, \partial h_2/\partial \xi_1)$ can be approximated by differences in grid edge lengths $(\Delta_2 h_1, \Delta_1 h_2)$. Therefore, as an example, the components of the strain increment for the southwest corner of a cell are given by

$$\begin{aligned}
\Delta\varepsilon_{11}^{sw} &= \dot{\varepsilon}_{11}^{sw}\Delta t = \frac{1}{\bar{h}_1\bar{h}_2}\left(\bar{h}_2(u^{se} - u^{sw}) + \Delta_2 h_1 v^{sw}\right)\Delta t \\
\Delta\varepsilon_{22}^{sw} &= \dot{\varepsilon}_{22}^{sw}\Delta t = \frac{1}{\bar{h}_1\bar{h}_2}\left(\bar{h}_1(v^{nw} - v^{sw}) + \Delta_1 h_2 u^{sw}\right)\Delta t \\
\Delta\varepsilon_{12}^{sw} &= \dot{\varepsilon}_{12}^{sw}\Delta t = \frac{1}{2}\frac{1}{\bar{h}_1\bar{h}_2}\left(\bar{h}_1(u^{se} - u^{sw}) - \Delta_2 h_1 u^{sw} + \bar{h}_2(v^{se} - v^{sw}) - \Delta_1 h_2 v^{sw}\right)\Delta t.
\end{aligned} \tag{21}$$

For each cell corner the stress is computed from the strain increments using the following algorithm. First, a trial stress $(\boldsymbol{\sigma}^{tr})$ is computed from the strain increment and the value of stress at the previous time step $(\boldsymbol{\sigma}^k)$ as

$$\boldsymbol{\sigma}^{tr} = \boldsymbol{\sigma}^k + \mathbb{E} : \Delta\boldsymbol{\varepsilon}. \tag{22}$$

If there is no active crack (*i.e.* $[\![\, \mathbf{u} \,]\!] = 0$) then a failure direction is chosen by maximizing the failure function over all possible crack directions. Once a failure direction is chosen, the failure

function is evaluated for values of the trial stress. If $F(\boldsymbol{\sigma}^{tr}) < 0$ then the step is elastic and the new stress is set to the trial stress ($\boldsymbol{\sigma}^{k+1} = \boldsymbol{\sigma}^{tr}$). If $F(\boldsymbol{\sigma}^{tr}) \geq 0$ then decohesion is occuring the decohesive strain $\boldsymbol{\varepsilon}^d$ required to return $F(\boldsymbol{\sigma})$ to zero must be found.

In order to solve this problem numerically, the singularity in the decohesive strain must first be regularized. We use a smeared-crack approach where the delta function in Eq. (16) is regularized over a computational element and replaced with an expression of the form

$$\boldsymbol{\varepsilon} = \overline{\boldsymbol{\varepsilon}} + \boldsymbol{\varepsilon}^d = \overline{\boldsymbol{\varepsilon}} + \frac{1}{L}(\llbracket \mathbf{u} \rrbracket \otimes \mathbf{n})^s. \tag{23}$$

The quantity L is a length scale related to the cell size that comes into the equation from the regularization of δ_Γ. This length scale is chosen to insure that the correct energy is dissipated during fracture [31]. Another dimensional parameter that influences the EDC rheology is the length scale u_0 which determines the width at which the crack is fully open and the traction on the surface has reduced to zero. The grid cell size varies over the displaced pole grid used in CICE, however the value of u_0 in other implementations has been set to be a constant for the entire grid. In our implementation we have chosen to set the ratio of u_0 to L to a constant so that both length scales vary depending on the grid cell size in a consistent manner.

Using the regularized decohesive strain, we employ Newton's method to solve for $F(\boldsymbol{\sigma}) = 0$ given that $\Delta\sigma = \mathbb{E} : (\Delta\varepsilon - \Delta\varepsilon^d)$. In the CICE implementation multiple cracks per cell with varying orientation are allowed. If additional cracks are active in the cell the procedure is repeated for the additional crack directions.

The CICE model uses explicit time stepping for the dynamics. Due to the potentially high viscosities in the EVP model the dynamics are typically subcycled with 120 subcycles for every 1 thermodynamic step. Subcycling is also used in the EDC implementation, however, the EDC model is stable for a larger time step so 60 subcycles have been used. At the end of the dynamic subcycling step values of the displacement jump orientations and directions are averaged over a cell. The averaged values are then advected using an incremental remap transport algorithm for tracer quantities, which is documented in [25]. At the next dynamics step the cell averaged jump and direction are used for the four corners of the cell.

4 Sensitivity Analysis

After the EDC model was implemented and tested in CICE, a sensitivity analysis was done to determine the impact of rheologic and dynamic parameters of the model on overall ice drift and deformation. For this analysis a two month run of CICE was performed for the months of January and February 1997 on a one degree global displaced pole grid (gx1). Atmospheric data from the Common Ocean-ice Reference Experiments (CORE) version 2 [24], which have been mapped to the gx1 grid, are used to drive the simulations. The data include spatially varying six-hourly atmospheric winds, specific humidity, and air temperature. Monthly spatially varying cloud fractions are taken from the Ocean Model Intercomparison Project (OMIP) data [29]. The downward longwave flux from the atmosphere is then derived from the air temperature and cloud fraction using the approach in [15]. Linear interpolation in time is used to derive the forcing for a given time step.

Spatially and seasonally varying ocean currents, sea surface salinity and sea surface temperature are taken from 20 year monthly means of POP ocean model output [32]. The sea ice velocity and thickness distribution are initialized with a standard CICE intialization file. Initial cracks for the EDC model are inferred from the strain rates derived from the initial ice velocity.

Parameters of interest for the sensitivity analysis were chosen from the set of material parameters used in the elastic-decohesive constitutive model and are shown the Table 8 with the sampling ranges used. All of the parameters were treated as having uniform distributions over the sampling range. The first two parameters, Young's modulus (E) and Poisson ratio (ν), define the isotropic elastic response of the material. These parameters are related to μ and λ in Eq. 18 as

$$\lambda = \frac{E\nu}{(1+\nu)(1-2\nu)}, \qquad \mu = \frac{E}{2+2\nu}. \tag{24}$$

The next three parameters, tensile (τ_{nf}), shear ($\tau_t f$), and compressive (f_c') strength determine the failure response of the material. The final two parameters are multiplicative factors that modify other responses. The shear multiplication factor modifies the shear failure condition under large compression and the opening parameter multiplication factor implicitly controls the material parameter that determines when a crack is fully open u_0.

Table 1: Model Parameters for Sensitivity Analysis.

Parameter	Range	Description
E	7.5×10^5 - 1.5×10^6	Young's Modulus
ν	0.33 - 0.36	Poisson Ratio
τ_{nf}	2.5×10^3 - 2.5×10^4	Tensile Strength
τ_{tf}	2.5×10^3 - 2.5×10^4	Shear Strength
f_c'	1.0×10^5 - 1.5×10^5	Compressive Strength
sm	2-8	Shear multiplication factor
u_{0fac}	3-6	Opening parameter multiplication factor

The response functions for the sensitivity analysis, listed in Table 2, were chosen either because they are bulk properties that are used to assess the state of the Arctic ice pack or because they are

useful in evaluating the model performance in terms of ice motion and deformation. The first three scalar fields are total Arctic ice extent, total Arctic ice volume, and root mean square ice speed, which are diagnostic output from the CICE model. The following four scalar fields are derived from model spatially varying velocity and deformation fields in comparison with satellite data.

The velocity error ($\mathbf{v}_{error}$) is a measure of the deviation of the model average velocity for February 1997 from satellite derived average velocity for February 1997. The satellite data are two day optimally interpolated ice motion fields derived from passive microwave instruments and buoy motions [18] and can be downloaded from `http://rkwok.jpl.nasa.gov/icemotion/index.html`. The model velocities are projected to a polar stereographic grid then interpolated to the 100 km resolution grid used by the passive microwave velocity data. The l^2 error in projected and interpolated model velocity $\mathbf{v} = (u, v)$ versus satellite velocity $\bar{\mathbf{v}} = (\bar{u}, \bar{v})$ is then computed as

$$\mathbf{v}_{error} = \frac{\left(\sum_i \left((u_i - \bar{u}_i)^2 + (v_i - \bar{v}_i)^2\right)\right)^{1/2}}{\left(\sum_i \left(\bar{u}_i^2 + \bar{v}_i^2\right)\right)^{1/2}}. \tag{25}$$

The final three response functions are the result of a comparison between model deformation measures and deformation measures derived from satellite data. The model divergence, vorticity, and shear are computed internally in CICE from the strain rate tensor as

$$\begin{aligned} D_d &= \dot{\varepsilon}_{11} + \dot{\varepsilon}_{22} \\ D_v &= \dot{\varepsilon}_{21} - \dot{\varepsilon}_{12} \\ D_s &= \sqrt{\left(\dot{\varepsilon}_{11} - \dot{\varepsilon}_{22}\right)^2 + \left(\dot{\varepsilon}_{12} - \dot{\varepsilon}_{21}\right)^2}. \end{aligned} \tag{26}$$

Deformation data for comparison are synthetic Aperture Radar (SAR) maps of the Arctic from RADARSAT, which are processed by the RADARSAT Geophysical Processor System (RGPS) developed at the Jet Propulsion Laboratory (JPL) [19, 21]. Area and feature-based tracking are used to generate ice displacements over time for an initially regular set of points. The resulting motion is used to compute deformation measures such as divergence, shear, and vorticity. The data are available for download at `http://rkwok.jpl.nasa.gov/radarsat/index.html`. To compute deformation correlations, the model data are first projected onto a polar stereographic grid then interpolated to the RGPS grid. Data are not available for all points at all times so comparison are only done at points where RGPS data are not missing. To assess the similarity between the model and RGPS deformations correlation coefficients are computed using the Matlab function `corrcoef`. The correlation computations are done for the net deformation for a three day period in February 1997.

The sampling-based sensitivity analysis was performed with the Design Analysis Kit for Optimization and Terascale Applications (DAKOTA) toolkit [1]. We implemented a Monte Carlo analysis based on Latin Hypercube Sampling (LHS) as in [27]. For this analysis 50 LHS were taken. A linear regression model was used evaluate the sensitivity of the response functions to the parameters. Given responses y_i for $i = 1, ..., 50$ input values and instantiations of the parameters x_{ij} $(j = 1, ...10)$ for each sample, the model can be algebraically formulated as

$$(y - \bar{y})/\hat{s} = \sum_j \frac{(a_j \hat{s}_j/\hat{s})(x_j - \bar{x}_j)}{\hat{s}_j}, \tag{27}$$

Table 2: Response Functions for Sensitivity Analysis.

Variable	Description
E_{tot}	Total ice extent (km^2)
V_{tot}	Total ice volume (m^3)
$\mathbf{v}_{rms}$	RMS ice speed (m/s)
$\mathbf{v}_{error}$	Velocity error
$D_{d,correl}$	Divergence correlation
$D_{v,correl}$	Vorticity correlation
$D_{s,correl}$	Shear correlation

where

$$\bar{y} = \sum_i \frac{y_i}{m}, \hat{s} = \Big(\sum_i \frac{(y_i - \bar{y})^2}{(m-1)}\Big)^{1/2}, \qquad \bar{x}_j = \sum_i \frac{x_{ij}}{m}, \hat{s}_j = \Big(\sum_i \frac{(x_{ij} - \bar{x}_j)^2}{(m-1)}\Big)^{1/2}. \tag{28}$$

The coefficients $a_j \hat{s}_j / \hat{s}$ are standardized regression coefficients with scaled values in the range of -1 to 1. When the x_j are independent, the absolute value of the standardized regression coefficients can be used to provide a measure of variable importance with respect to observed uncertainty in the response function.

Standardized regression coefficients from the sensitivity analysis are provided in Table 3. Of the 50 LHS only 39 ran to completion and therefore the sensitivity results include only these 39 complete cases. Values greater than 0.3 are displayed in bold font and indicate a fairly significant relationship between the parameter and the response function. These results suggest that the values of the shear multiplication factor (s_m), the Poisson ratio (ν), and the compressive strength (f'_c) do not have much impact on the selected responses. The Arctic sea ice extent and volume at the end of the run are both strongly influenced by the tensile strength (τ_{nf}), where a negative value for the coefficient indicates that the extent and volume increase as the tensile strength decreases. This relationship is intuitively reasonable for the ice extent, where a larger extent can be obtained dynamically as the ice breaks up and spreads apart. The tensile strength can have an impact on ice volume by increasing the number of cracks with exposed open water in the winter that freeze and thereby increase the total volume of ice. It is likely that the opening factor $u_{0,fac}$ contributes the ice volume in a similar manner by influencing how much open water is available to freeze and ridge.

The root mean square ice speed is influenced by the tensile strength, shear strength, and Young's modulus, where lower values of the Young's modulus and the strength terms contribute to greater RMS speed in the Arctic. The error in the averaged February 1997 velocity shows a more complicated dependence on parameters where the error decreases with increasing Young's modulus and increases with increasing shear strength. The divergence correlation is moderately influenced by Young's modulus and the tensile strength, while the vorticity correlation is strongly influenced by the shear strength and the shear modulus is moderately influenced by Young's modulus.

Although the standardized regression coefficients show that the Young's modulus has a moderate influence on RMS speed, velocity error, divergence correlation, and shear correlation, the largest influences on the response functions appear to be from the shear and tensile strengths.

Table 3: Standardized regression coefficients from the 2 month sensitivity analysis using 1997 forcing for 39 valid samples. Significant values (> 0.3) are indicated in bold font.

Parameter	Extent	Volume	RMS Speed	Velocity Error	Divergence Correlation	Vorticity Correlation	Shear Correlation
E	0.0678	0.0652	**-0.331**	**-0.403**	**-0.394**	-0.0994	**-0.319**
ν	-0.0775	0.0706	-0.0393	0.00642	-0.136	-0.0132	-0.263
τ_{nf}	**-0.883**	**-0.931**	**-0.563**	-0.102	0.192	**-0.301**	0.0267
τ_{tf}	0.194	0.00283	**-0.601**	**0.411**	**-0.378**	**-0.833**	0.204
f_c'	0.104	-0.0598	0.00651	0.0591	-0.0958	-0.0388	0.0399
sm	-0.0648	0.129	-0.140	0.0463	-0.00968	-0.137	-0.174
u_0 Factor	-0.104	**-0.377**	-0.197	-0.267	-0.0861	-0.115	-0.131

The mean and standard deviation of the response functions from the 39 final samples are given in Table 4 along with results from a control run of the code using the EVP rheology with standard parameter values. The mean value of extent for the EDC samples is lower than the extent value for the EVP result. In contrast the EVP result for volume is lower than the EDC result for mean volume. The EVP result has higher root mean squared (RMS) speed. The mean EDC velocity error tends to be higher than the EVP velocity and the deformation correlations are generally stronger for EVP than EDC for this set of parameter values.

Table 4: Mean and standard deviation of response functions from two month sensitivity analysis using 1997 forcing. Results from the two month CICE run with EVP rheology is shown for comparison.

Response	EDC Sample Results		EVP Result
	Mean	Standard Dev.	
Extent	1.522×10^7	1.974×10^4	1.544×10^7
Volume	2.207×10^{13}	1.536×10^{11}	2.171×10^{13}
RMS Speed	0.09792	0.005970	0.1172
Velocity Error	0.8276	0.0123	0.7103
Divergence Correlation	0.1427	0.02530	0.2572
Shear Correlation	0.07824	0.0764	0.2648
Vorticity Correlation	0.1331	0.02129	0.1380

A visual comparison between one set of sample results and the deformation data is provided in Figure 3 where plots of divergence, vorticity, and shear for February 17-19 1997 are shown for the RGPS data, the EVP model results, and EDC model results for sample number 11. This sample was chosen because it produced relatively high deformation correlations of 0.165, 0.210, and 0.177 for divergence, vorticity, and shear respectively. Parameter values for sample 11 are provided in Table 5. Both the EDC and EVP model underpredict the divergence, but there are some features in common between the data and model results for the vorticity and shear.

Velocity comparisons between model and data are shown in Figure 4. In this case results from sample number 17 are shown. This sample produced the lowest velocity error of 0.781. As

indicated by the RMS velocity values the EDC rheology produces lower average velocities than the EVP rheology particularly through the Fram strait and along the East coast of Greenland. In the cases of both EDC and EVP models, the ice motion is smaller than what is seen in the data along the Alaskan coast.

Table 5: Parameter values for two samples with low velocity error and high deformation correlations.

Parameter	Sample 11	Sample 17
E	1.2603153e+06	1.3487883e+06
ν	3.3091461e-01	3.4621522e-01
τ_{nf}	1.1974861e+04	1.2545249e+04
τ_{tf}	5.0078342e+03	2.5106544e+03
f_c'	1.0855310e+05	1.3153122e+05
sm	4.3558734e+00	4.1162674e+00
u_0 Factor	3.7331775e+00	5.8942635e+00

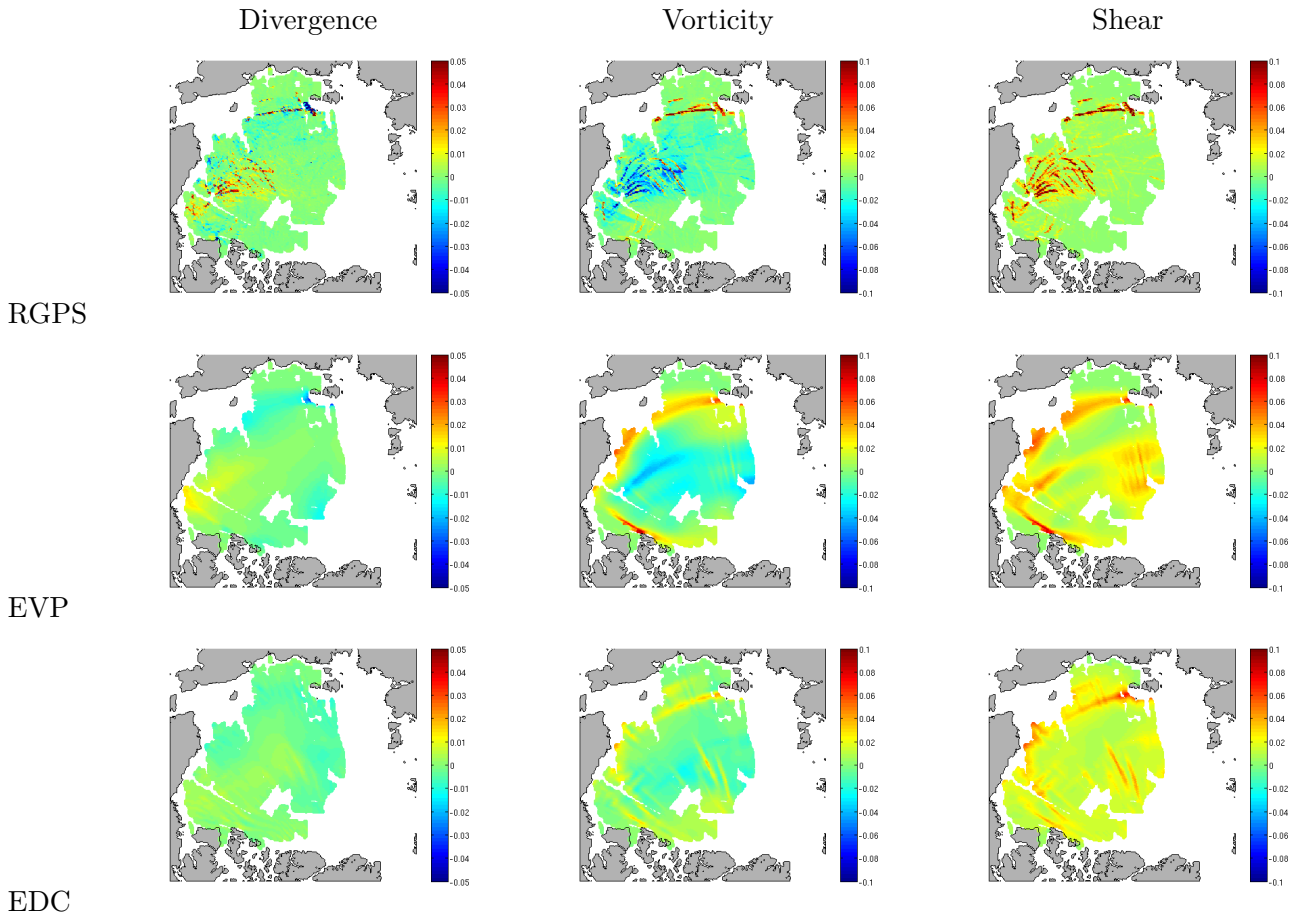

Figure 3: Plot of divergence, vorticity and shear for three days in February 1997 from RGPS and CICE simulation runs. Results from the CICE simulations were projected onto a polar stereographic grid and interpolated to the RGPS grid with resolution 12 km. Points where RGPS data are not available are not shown.

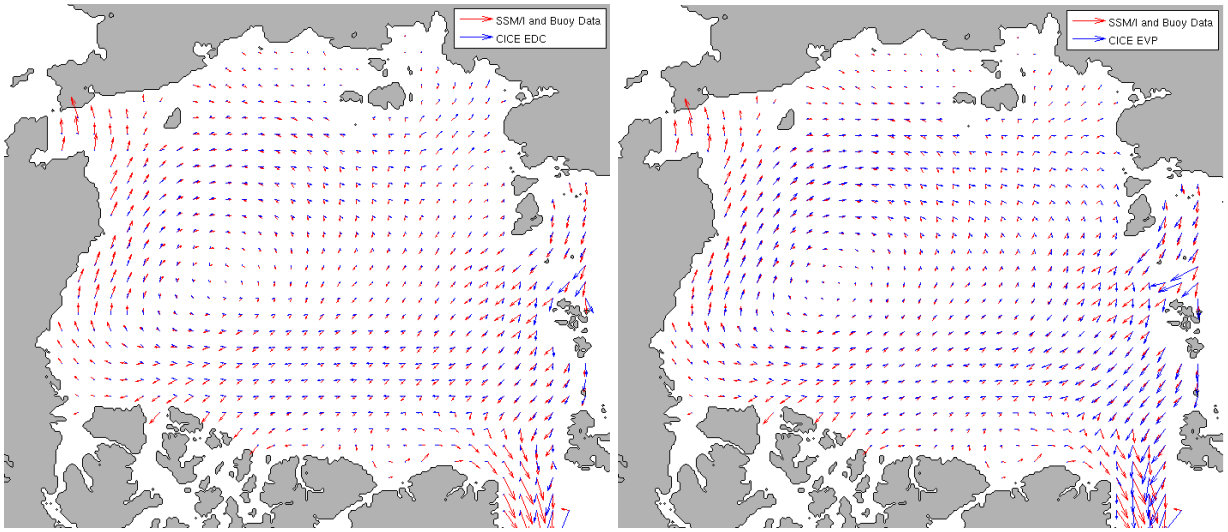

Figure 4: February 1997 averaged optimally interpolated buoy and SSM/I ice motion (red arrows) compared with results displayed as blue arrows from EDC (left) and EVP (right) rheologies.

5 Optimization

Based on the results of the sensitivity study, a new set of samples was obtained using the same response functions for only two parameters τ_{nf} and τ_{tf}. In this analysis 2004 forcing was used with the same initial conditions and a two month (January/February) run was completed. Of the 50 LHS runs, two failed to complete leaving 48 samples for the analysis. Standardized regression coefficients in Table 6 show similar behavior to what was seen in the 1997 sensitivity study. The ice extent and volume appear to be influenced primarily by τ_{nf} where lower values increase the extent and volume. The RMS speed shows a moderate dependence on both material parameters such that lower tensile and shear strength results in higher RMS speed. The vorticity correlation is particularly strong for τ_{tf} where lower values produce a better vorticity correlation.

Table 6: Standardized regression coefficients from the two month sensitivity analysis with 2004 forcing. Significant values in bold font.

Parameter	Extent	Volume	RMS Speed	Velocity Error	Divergence Correlation	Vorticity Correlation	Shear Correlation
τ_{nf}	**-0.883**	**-0.9310**	**-0.563**	**-0.683**	0.194	-0.301	0.0857
τ_{tf}	0.194	0.0028	**-0.601**	0.252	-0.376	**-0.833**	0.265

In Table 7 the mean and standard deviations for the 2004 analysis are shown along with results for a two month CICE run for comparison. In this case the mean divergence, shear, and vorticity correlation are poor especially compared with the relatively high values from the EVP model. However the mean velocity error of the EDC model is noticably better than for the EVP model. Plots of ice deformation from RGPS data, EVP model results, and EDC model results for sample 31 with $\tau_{nf} = 2.4145888 \times 10^4$ and $\tau_{tf} = 4.2705908 \times 10^3$ are shown in Figure 5. Although on average the samples show poor correlation with the deformation measures, sample 31 has correlations of 0.3595 and 0.2281 for the vorticity and shear respectively. The overall deformation in the figures is not unreasonable, although there appears to be too much shear deformation and an underprediction of divergence. Ice motion comparisons between model results and data are shown in Figure 6. The EDC model results are for sample 35 with $\tau_{nf} = 9.6725619 \times 10^3$ and $\tau_{tf} = 3.7109641 \times 10^3$, which produced a velocity error of 0.4959. The EVP model velocities are generally higher than the data for this particular case, while the EDC velocities are much closer.

Results in Table 6 indicate that the tensile strength has a strong influence on sea ice extent and volume while the shear strength has a strong influence on the correlation to deformation measures. This is supported by looking at the influence of the two parameters on an error measure that combines ice motion and deformation. Since we would like to reduce the ice velocity error and increase the divergence, vorticity, and shear correlation an appropriate measure is

$$J = v_{error} + (1 - D_{d,correl})^2 + (1 - D_{v,correl})^2 + (1 - D_{s,correl})^2. \tag{29}$$

Evaluating the error measure for each valid sample producing a scatter plot for each parameter displays a striking pattern. As shown in Figure 7 the error decreases significantly for decreasing τ_{tf}, but does not show a clear dependence on τ_{nf}.

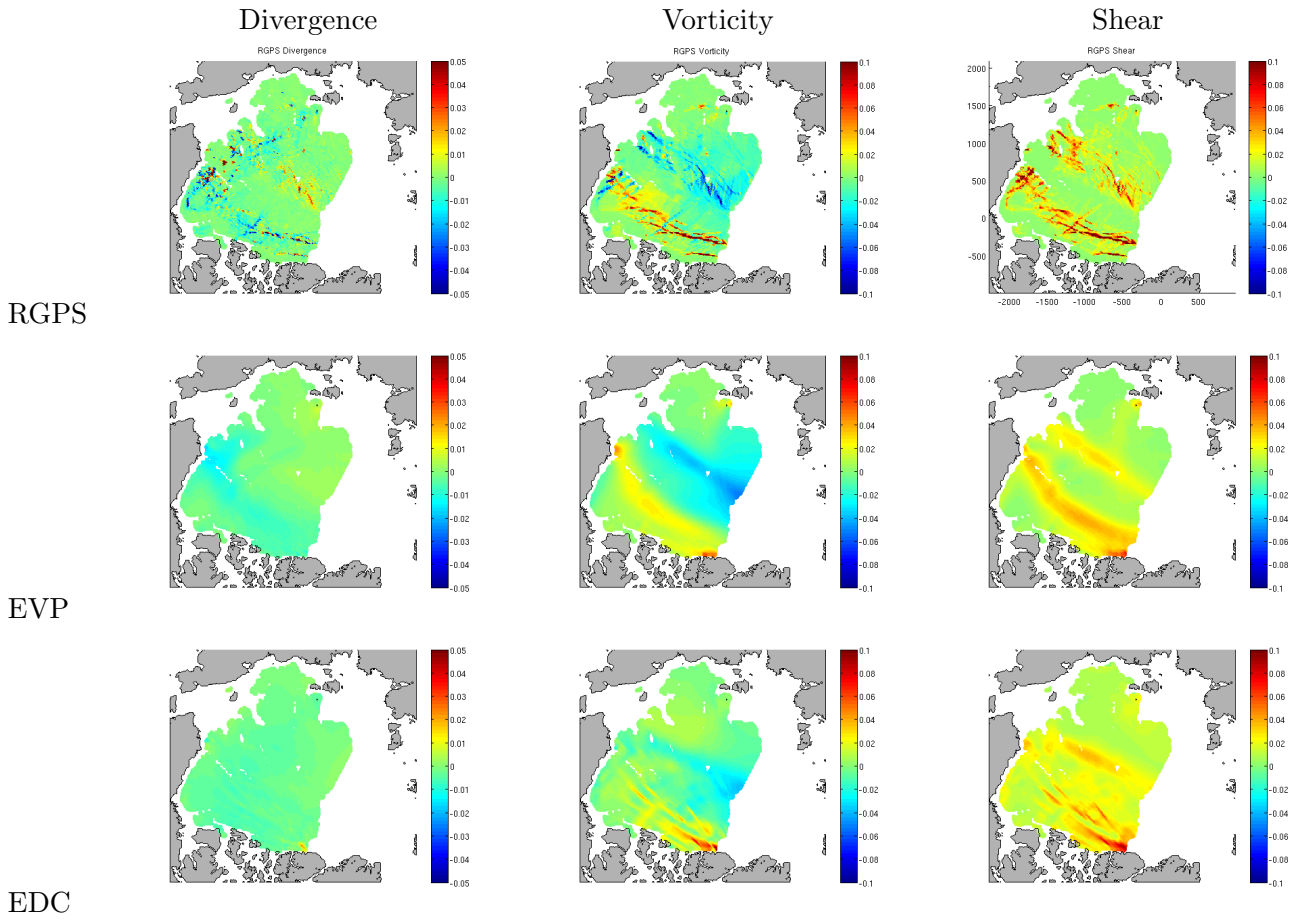

Figure 5: Plot of divergence, vorticity and shear for three days in February 2004 from RGPS and CICE simulation runs. Results from the CICE simulations were projected onto a polar stereographic grid and interpolated to the RGPS grid with resolution 12 km.

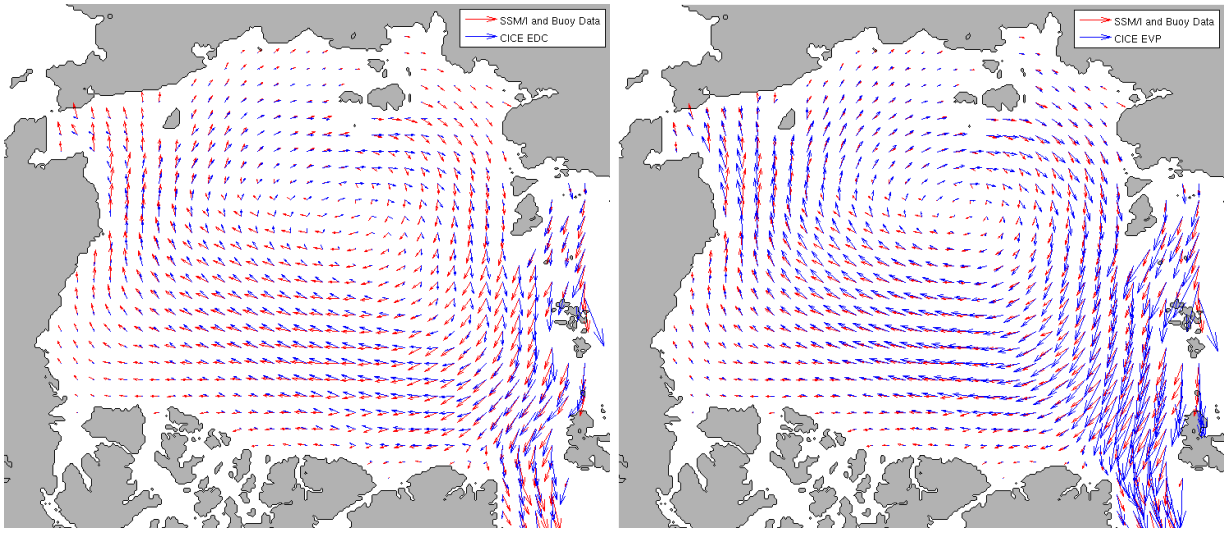

Figure 6: February 2004 averaged optimally interpolated buoy and SSM/I ice motion (red arrows) compared with results displayed as blue arrows from EDC (left) and EVP (right) rheologies.

Table 7: Mean and standard deviation of response functions from 2 month sensitivity analysis with 2004 forcing. Results from 2004 two month CICE run with EVP rheology shown for comparison.

Response	EDC Sample Results		EVP Result
	Mean	Standard Dev.	
Extent	1.523×10^7	2.101×10^4	1.539×10^7
Volume	2.161×10^{13}	1.256×10^{11}	2.309×10^{13}
RMS Speed	0.0884	0.00491	0.1071
Velocity Error	0.6544	0.0845	0.8450
Divergence Correlation	-0.00346	0.0427	0.0627
Shear Correlation	-0.0718	0.1984	0.4187
Vorticity Correlation	0.0679	0.07268	0.3374

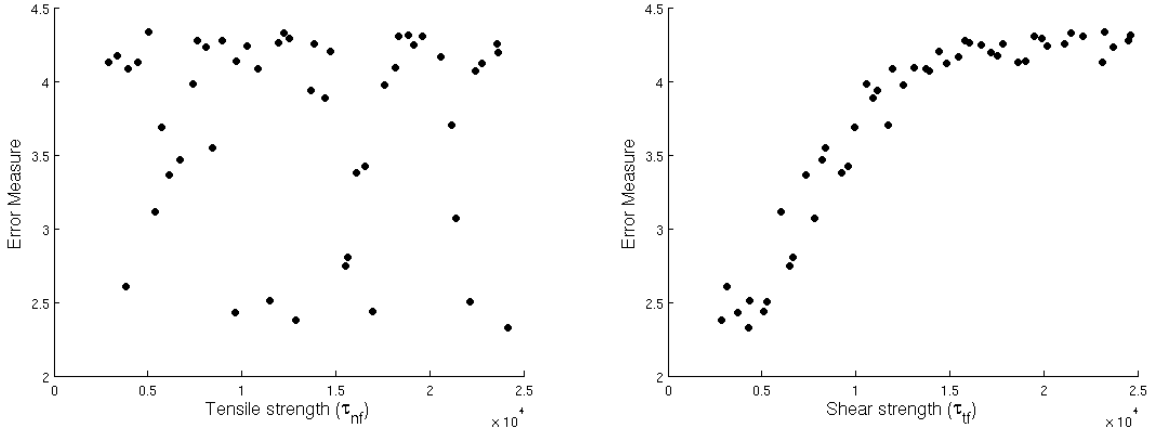

Figure 7: Scatter plots of samples results for ice deformation and motion error versus parameter. The error decreases significantly for decreasing τ_{tf}, but does not show a clear dependence on τ_{nf}.

6 Ten Year Model Run

In order to evaluate long-term behavior of the EDC rheology, ten year CICE model runs were performed for the years 1995 through 2004. As before monthy average ocean data was used along with six-hourly atmospheric data for 1995-2004 from [24] to drive the simulations.

Variations in Arctic sea ice extent and volume over the ten year run are shown in Figures 8 and 9. The extent values are compared with monthly averaged sea ice extent from the National Snow and Ice Data Center (NSIDC) [6]. For both the EDC and EVP rheology the matches with the ice extent data are fairly good, although it appears that the EVP model results tend to have slightly lower extents than EDC in the summer months. The Arctic volume values are compared with data from the Pan-Arctic Ice Ocean Modeling and Assimilation System (PIOMAS) [39]. Because the ice thickness was not initialized to match 1995 thickness data it is not expected that the total Arctic volume values will match exactly. Therefore, it is more important that a reasonable trend is seen. Results for the EVP rheology do show a reasonable trend over the ten year period, but the EDC results shown an increase in volume over the same time frame.

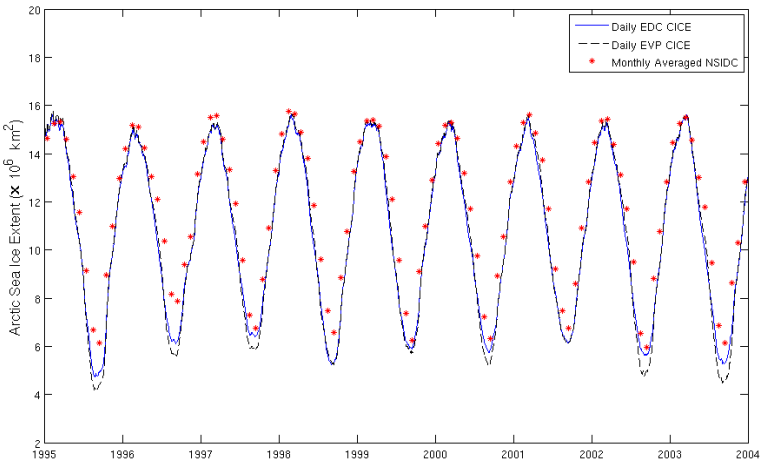

Figure 8: Daily ice extent from CICE simulations compared with monthly averaged National Snow and Ice Data Center (NSIDC) ice extent. The minimum ice extent is lower in the CICE EVP run than in the CICE ECD run and data.

Consistent with the ice volume trends shown in Figure 9, the ice thickness in the final year is much higher for the EDC rheology than the EVP rheology. The average thickness for the months of February and March are displayed in Figure 10 and compared with Ice, Cloud, and land Elevation Satellite (ICESat) thickness data for the same period. The ICESat thickness data for February and March 2004 are derived from lidar sea ice elevation profiles from a single ICESat campaign [20] and can be downloaded from `http://rkwok.jpl.nasa.gov/icesat/index.html`. The thickness values for the computation were averaged over the two months and then projected onto a polar stereographic grid and interpolated to the ICESat data points for comparison. The volume of ice represented by the ICESat data can be approximated by summing up the thickness at each point multiplied by the area resolution of 25 $\times$ 25 km^2 and is found to be 1.653 $\times 10^{13}$ m^3. Using the same method for the interpolated model data the EVP volume is 1.329 $\times 10^{13}$ m^3, and the EDC volume is 2.035

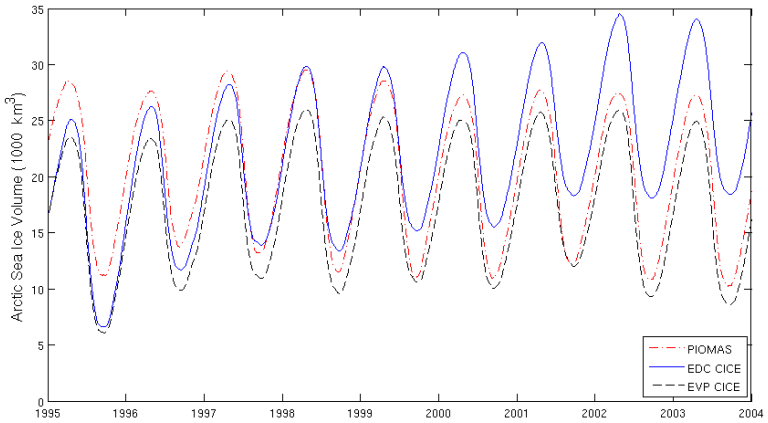

Figure 9: Daily ice volume from CICE simulations compared with PIOMAS ice volume estimates. While the CICE EVP run has lower ice volume than the PIOMAS estimates for this ten year period, the trends appear reasonable. However, the CICE EDC is clearly producing too much ice growth possibly due to the EDC algorithm interactions with the ridging model.

$\times 10^{13}$ m^3. As is apparent in Figure 10 the EDC model overestimates the ice thickness and volume and the EVP model tends to underestimate the thickness and volume.

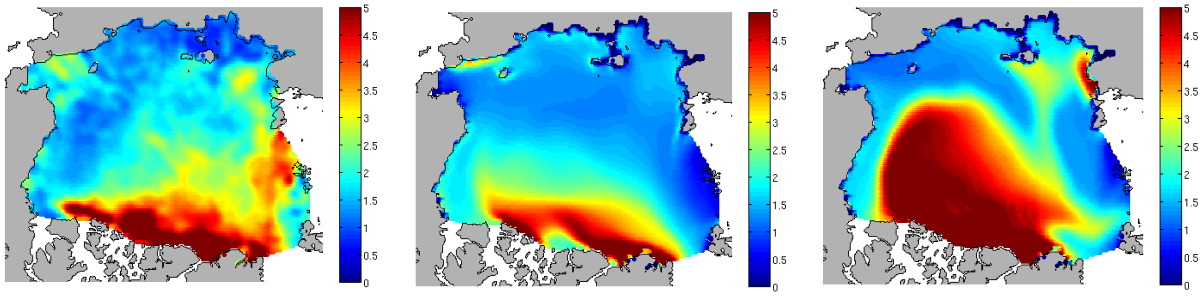

(a) (b) (c)

Figure 10: Average February/March 2004 ice thickness from ICESAT data (a), CICE with EVP (b), CICE with EDC (c).

Plots of averaged ice velocity over 1995-2004 for the months of December, January, and February are shown in Figure 11. As seen before, the EDC rheology results have lower average velocity than results for the EVP rheology, where the velocity through the Fram Strait and along the eastern coast of Greenland is overestimated. The EDC model produces smaller velocities in the Arctic interior that are smaller on average than the data, but produces more reasonable results along the Greenland coast. Overall the average velocity errors shown in Table 8 for the EDC rheology are slightly lower than the velocity errors for the EVP rheology. Both rheologies underestimate motion and deformation along the Alaskan coast as was seen in the previous sensitivity analysis and in [22].

Plots of divergence, vorticity and shear averaged over the month of February 2004 are given in Figure 12. As seen before the divergence is underpredicted by both model rheologies. The vorticity

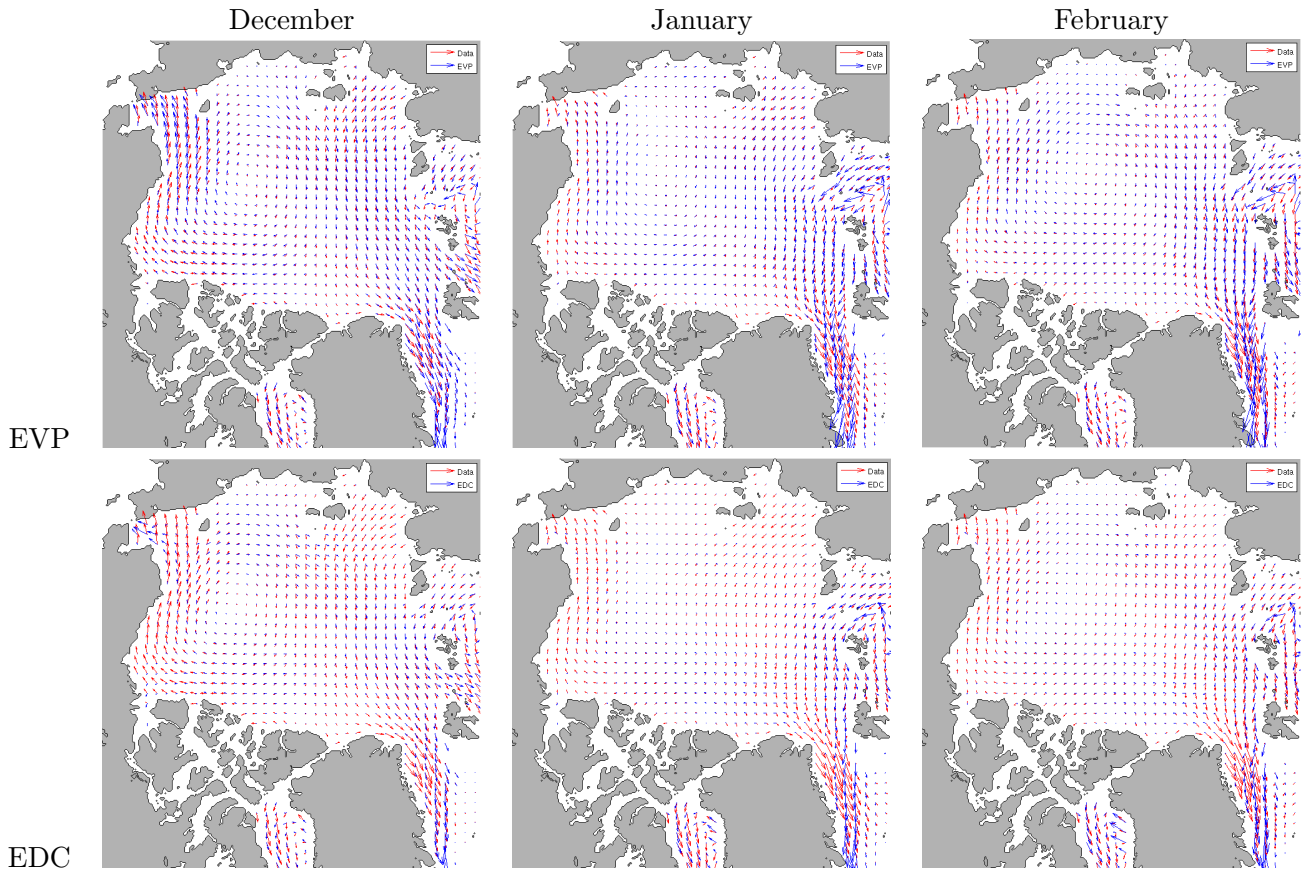

Figure 11: 1995-2004 averaged optimally interpolated buoy and SSM/I ice motion (red arrows) compared with results from ten year model run with EDC and EVP rheologies (blue arrows) for the months of December, January, and February.

Table 8: January, February, and March averaged velocity errors for the 1995-2004 runs with EVP and EDC rheologies. The EDC model produces lower velocities on average than the EVP model with a better match to the RMS velocity of the data, which is the reason for the somewhat lower velocity errors for EDC versus EVP.

Month	EVP		EDC		Data
	RMS Vel (m/s)	l_2 Error	RMS Vel (m/s)	l_2 Error	RMS Vel (m/s)
December	0.0532	0.956	0.0350	0.936	0.0395
January	0.0620	1.366	0.0451	1.202	0.0367
February	0.0667	1.283	0.0460	1.052	0.0410

for both EVP and EDC exhibits some features that seem similar to the data, however, the negative vorticity seems to be underpredicted especially along the Alaskan coast. Results for shear from the EVP rheology are similar in that they underpredict deformation along the coast of Alaska, however results from the EDC rheology clearly show an excess of shear particularly along the Canadian coast.

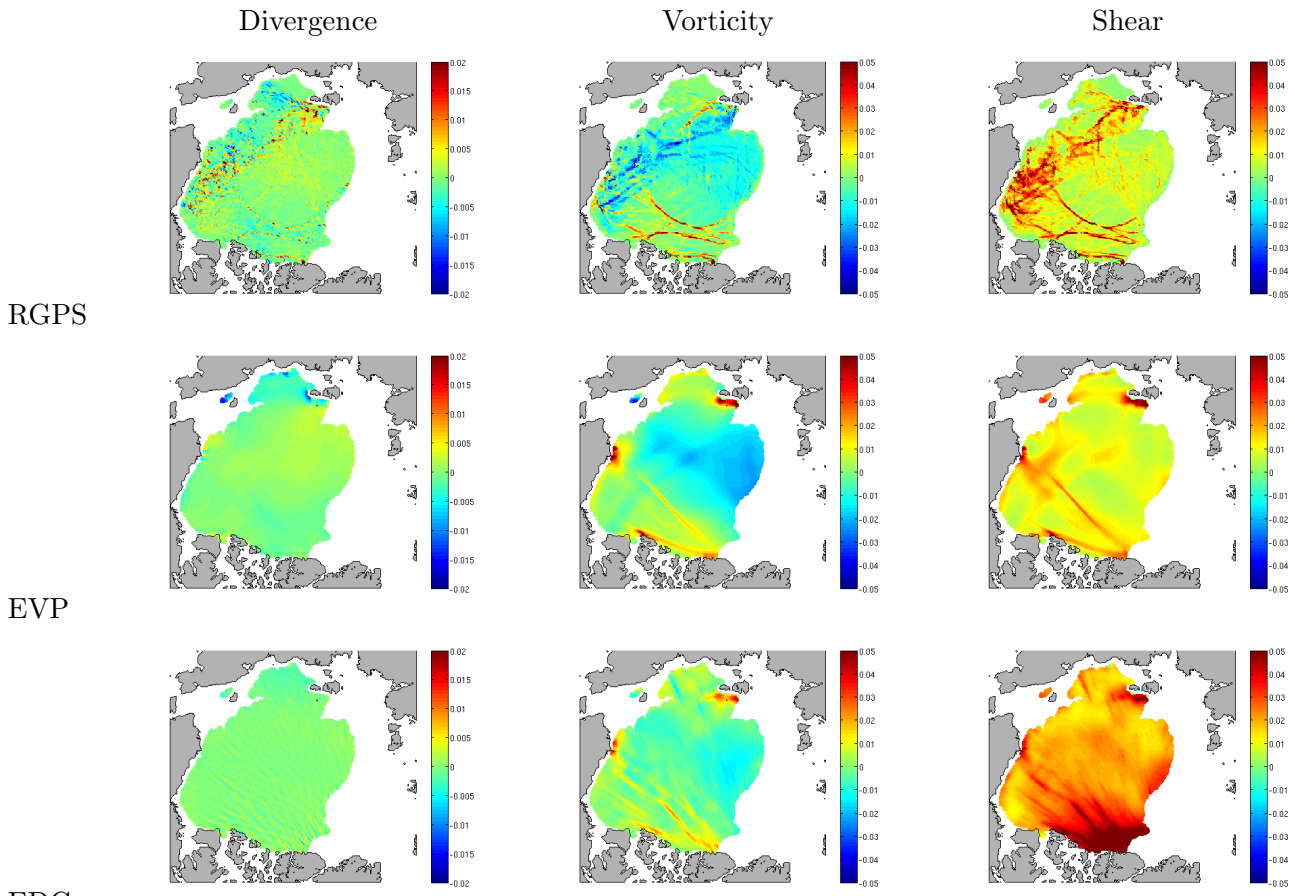

Figure 12: Divergence, vorticity and shear averaged for February 2004 from RGPS and CICE simulation runs. Results from the CICE simulations were projected onto a polar stereographic grid and interpolated to the 12 km resolution RGPS data grid.

7 Conclusions

The elastic-decohesive anisotropic rheology has been incorporated into the LANL CICE code. Sensitivity analyses were performed to determine the effect of rheologic parameters on response functions such as ice volume, ice extent, ice speed, and correlations with deformation measures. Additional samples with variations in the two most significant parameters (tensile strength and shear strength) suggest that reducing the shear strength has the most impact on matching ice motion and deformation.

A ten year run was completed to assess the performance of the EDC rheology for longer time scales. Results indicate that the EDC rheology produces lower average velocities than the EVP rheology, which can result in a better match with the data especially for velocities in the region of the Fram Strait. However, the ice thickness increases too much over the ten year run for the EDC rheology, suggesting that interactions with the ridging routine and dynamics are causing too much new ice to form. One limitation with the EDC model is the assumption of zero crack closing strength. A possible next step is to implement the proposed closing algorithm from [31], which would potentially reduce the amount of closing and therefore reduce the amount of ice ridging.

References

[1] B. M. Adams, W. J. Bohnhoff, K. R. Dalbey, J. P. Eddy, M. S. Eldred, D. M. Gay, K. Haskell, P. D. Hough, and L. P. Swiler. DAKOTA, a multilevel parallel object-oriented framework for design optimization, parameter estimation, uncertainty quantification, and sensitivity analysis: Version 5.0 user's manual. Technical Report SAND2010-2183, Sandia National Laboratories, 2009.

[2] C. M. Bitz and W. H. Lipscomb. An energy-conserving thermodynamic model of sea ice. *Journal of Geophysical Research*, 104(C7):15669–15677, 1999.

[3] J. C. Comiso, C. L Parkinson, R. Gersten, and L. Stock. Accelerated decline in the Arctic sea ice cover. *Geophysical Research Letters*, 35:L01703, 2008.

[4] M. Coon, R. Kwok, G. Levy, M. Pruis, H. Schreyer, and D. Sulsky. Arctic ice dynamics experiment AIDJEX assumptions revisited and found inadequate. *Journal of Geophysical Research*, 112:C11S90, 2007.

[5] M. D. Coon, G. S. Knoke, and D. C. Echert. The architecture of an anisotropic elastic-plastic sea ice mechanics constitutive law. *Journal of Geophysical Research*, 103:21915–21925, 1998.

[6] F. Fetterer, K. Knowles, W. Meier, and M. Savoie. Sea ice index. *Boulder, Colorado, USA, National Snow and Ice Data Center. Digital Media*, 2002, updated 2009.

[7] J.A. Francis and S.Vavrus. Evidence linking Arctic amplification to extreme weather in mid-latitudes. *Geophysical Research Letters*, 39:L06801, 2012.

[8] C. A. Geiger, W. D. Hibler, and S. F. Ackley. Large-scale sea ice drift and deformation: Comparison between models and observations in the western weddel sea during 1992. *Journal of Geophysical Research*, 103:21893–21913, 1998.

[9] L. Girard, S. Bouillon, J. Weiss, D. Amitrano, T. Fichefet, and V. Legat. A new modeling framework for sea-ice mechanics based on elasto-brittle rheology. *Annals of Glaciology*, 52(57):123–132, 2011.

[10] L. Girard, J. Weiss, J. M. Molines, B. Barnier, and S. Bouillon. Evaluation of high-resolution sea ice models on the basis of statistical and scaling properties of Arctic sea ice drift and deformation. *Journal of Geophysical Research*, 114:C08015, 2009.

[11] J. M. N. T. Gray and L. W. Morland. A two-dimensional model for the dynamics of sea ice. *Philosophical Transactions: Physical Sciences and Engineering*, 347(1682):219–290, 1994.

[12] W. D. Hibler. A dynamic thermodynamic sea ice model. *Journal of Physical Oceanography*, 9:815–845, 1979.

[13] E. C. Hunke and J. K. Dukowicz. An elastic-viscous-plastic model for sea ice dynamics. *Journal of Physical Oceanography*, 27:1849–1867, 1997.

[14] E. C. Hunke and J. K. Dukowicz. The elastic viscous-plastic sea ice dynamics model in general orthogonal curvilinear coordinates on a sphere - incorporation of metric terms. *Monthly Weather Review*, 130:1848–1865, 2002.

[15] E. C. Hunke and M. M. Holland. Global atmospheric forcing data for Arctic ice-ocean modeling. *Journal of Geophysical Research*, 112:C04S14, 2007.

[16] E. C. Hunke and W. H. Lipscomb. CICE: the Los Alamos sea ice model documentation and software user's manual version 4.1. Technical Report LA-CC-06-012, Los Alamos National Laboratory, 2010.

[17] R. Kwok. Observational assessment of Arctic sea ice motion, export, adn thickness in CMIP3 climate simulations. *Journal of Geophysical Research*, 116:C00D05, 2011.

[18] R. Kwok, A.Schweiger, D. A. Rothrock, S. Pang, and C. Kottmeier. Sea ice motion from satellite passive microwave imagery assessed with ERS SAR buoy motions. *Journal of Geophysical Research*, 103(C4):8191–8213, 1998.

[19] R. Kwok and G. F. Cunningham. RADARSAT geophysical processor system data user's handbook. Technical report, JPL, 2000.

[20] R. Kwok, G. F. Cunningham, M. Wensnahan, I. Rigor, H. J. Zwally, and D. Yi. Thinning and volume loss of the Arctic ocean sea ice cover: 2003-2008. *Journal of Geophysical Research*, 114:C07005, 2009.

[21] R. Kwok, J.C. Curlander, R. McConnell, and S.S. Pang. An ice-motion tracking system at the Alaska SAR facility. *IEEE Journal of Oceanic Engineering*, 15:44–54, 1990.

[22] R. Kwok, E. C. Hunke, W. Maslowski, D. Menemenlis, and J. Zhang. Variability of sea ice simulations assessed with RGPS kinematics. *Journal of Geophysical Research*, 113:C11012, 2008.

[23] R. Kwok and D. A. Rothrock. Decline in Arctic sea ice thickness from submarine and icesat records 1958-2008. *Geophysical Research Letters*, 36:L15501, 2009.

[24] W. G. Large and S. G. Yeager. The global climatology of an interannually varying air-sea flux data set. *Climate Dynamics*, 2008.

[25] W. H. Lipscomb and E. C. Hunke. Modeling sea ice transport using incremental remapping. *Monthly Weather Review*, 132:1341–1354, 2004.

[26] W. H. Lipscomb, E. C. Hunke, W. Maslowski, and J. Jakacki. Ridging, strength, and stability in high-resolution sea ice models. *Journal of Geophysical Research*, 112:C03S91, 2007.

[27] K. Peterson, P. Bochev, and B. Paskaleva. Development, sensitivity analysis, and uncertainty quantification of high-fidelity Arctic sea ice models. Technical Report SAND 2010-6218, Sandia National Laboratories, 2010.

[28] P. Rampal, J. Weiss, C. Dubois, and J.-M. Campin. IPCC climate models do not capture Arctic sea ice drift acceleration: consequences in terms of projected sea ice thinning and decline. *Journal of Geophysical Research*, 116:C00D07, 2011.

[29] F. Roske. An atlas of surface fluxes based on the ECMWF reanalysis - a climatolgical dataset to force global ocean general circulation models. Technical report, Max-Planck Institut Fur Meteorologie, 2001.

[30] D. A. Rothrock. The energetics of the plastic deformation of pack ice by ridging. *Journal of Geophysical Research*, 80:4514–4519, 1975.

[31] H. Schreyer, L. Monday, D. Sulsky, M. Coon, and R. Kwok. Elastic-decohesive constitutive model for sea ice. *Journal of Geophysical Research*, 111:C11S26, 2006.

[32] R. Smith and P. Gent. Reference manual for the parallel ocean program (POP). Technical Report LAUR-02-2484, Los Alamos National Laboratories, 2002.

[33] H. L. Stern and R. W. Lindsay. Spatial scaling of Arctic sea ice deformation. *Journal of Geophysical Research*, 114:C10017, 2009.

[34] J. Stroeve, M. M. Holland, W. Meier, T. Scambos, and M. Serreze. Arctic sea ice decline: Faster than forecast. *Geophysical Research Letters*, 34(L09501):1–5, 2007.

[35] D. Sulsky and K. Peterson. Towards a new elastic-decohesive model of Arctic sea ice. *Physica D*, 240:1674–1683, 2011.

[36] D. Sulsky, H. Schreyer, K. Peterson, M. Coon, and R. Kwok. Using the material-point method to model sea ice dynamics. *Journal of Geophysical Research*, 112:C02S90, 2007.

[37] A.S. Thorndike, D.A. Rothrock, G.A. Maykut, and R. Colony. The thickness distribution of seaice. *Journal of Geophysical Research*, 80(33):4501–4513, November 1975.

[38] A. V. Wilchinsky and D. L. Feltham. A continuum anisotropic model of sea-ice dynamics. *Proc. R. Soc. Lond. A*, 460:2105–2140, 2004.

[39] J. Zhang and D. A. Rothrock. Modeling global sea ice with a thickness and enthalpy distribution model in generalized curvilinear coordinates. *Monthly Weather Review*, 131(5):681–697, 2003.

DISTRIBUTION:

1 Elizabeth Hunke
Los Alamos National Laboratory
MS-B216
Los Alamos, NM 87545

1 Deborah Sulsky
Department of Mathematics and Statistics
MSC03 2150
1 University of New Mexico
Albuquerque, NM 87131

1 MS 1318 Kara Peterson, 1442

1 MS 1320 Pavel Bochev, 1442

1 MS 0899 Technical Library, 9536 (electronic copy)

1 MS 0359 D. Chavez, LDRD Office, 1911


Sandia National Laboratories